

Abundance profiles in cooling-core clusters: a fossil record of past AGN-driven convection?

Y. Rasera, B. Lynch, K. Srivastava and B. Chandran

Space Science Center, University of New Hampshire, Durham, NH 03824, USA

yann.rasera@obspm.fr

ABSTRACT

Central peaks in the iron abundance of intracluster plasma are a common feature of cooling-core galaxy clusters. Although centrally localized, these abundance peaks have a much broader profile than the stars of the central brightest cluster galaxy (BCG), which produce the excess iron, indicating that metal-enriched plasma is transported out of the BCG by some process such as turbulent diffusion. At the same time, cooling-core clusters are likely heated by central active galactic nuclei (AGNs) by means of jets, cosmic-ray bubbles, and/or convection. The recent AGN-driven convection model of Chandran & Rasera predicts the turbulent velocity profile in a steady-state cluster in which radiative cooling is balanced by heating from a combination of AGN-driven convection and thermal conduction. We use the velocity profiles from this model as input into an advection/diffusion model for the transport of metals in the intracluster medium, taking the iron to be injected by the BCG. We compare the results of our model to XMM and Chandra observations of eight clusters. Assuming a constant turbulence level over a cluster's lifetime, the turbulent velocities in the model can explain the observed abundance profiles in only five of the eight clusters. However, we go on to develop an analytic fit of the turbulent velocity profile as a function of the AGN power. We then deduce for each cluster the average AGN power (during the past ~ 10 Gyr) required to match the abundance profiles. The required average values are between 10^{43} and 2×10^{44} erg.s $^{-1}$, while the present AGN powers span a much larger range from 6×10^{41} (Virgo) to 2×10^{44} erg.s $^{-1}$ (Hydra A). Our results suggest that AGN-driven convection can account for the observed abundance profiles if the AGN power varies over a cluster's lifetime between Virgo-like and Hydra-A-like values, with average values in the above-quoted range.

Subject headings: galaxies: abundances — diffusion — convection — galaxies: clusters: general — cooling flows — galaxies: elliptical and lenticular, cD — methods: analytical - galaxies: clusters: individual (Perseus, Hydra A, Sersic 159-03, Abell 262, Abell 1795, Virgo, Abell 496, Abell 4059)

1. Introduction

In many clusters of galaxies, the radiative cooling time at the cluster's center is much shorter than the cluster's age (Fabian 1994). Nevertheless, high-spectral-resolution X-ray observations show that very little plasma actually cools to low temperatures (Böhringer et al. 2001; David et al. 2001; Molendi & Pizzolato 2001; Peterson et al. 2001, 2003; Tamura et al. 2001b; Blanton et al. 2003). This finding, some times referred to as

the “cooling-flow problem,” strongly suggests that plasma heating approximately balances radiative cooling in cluster cores.

Although a number of different heat sources have been considered in the literature, there is growing interest in the role of central active galactic nuclei (AGNs). The importance of AGN heating or “AGN feedback” is suggested by the observation that almost all clusters with strongly cooling cores possess active central radio sources (Burns 1990; Ball et al. 1993; Eilek 2004) and

by the correlation between the X-ray luminosity from within a cluster's cooling radius and the mechanical luminosity of a cluster's central AGN (Bîrzan et al. 2004; Eilek 2004). One of the main unsolved problems regarding AGN feedback, however, is to understand how AGN power is transferred to the diffuse ambient plasma. A number of mechanisms have been investigated, including Compton heating (Binney & Tabor 1995; Ciotti & Ostriker 1997, 2001; Ciotti et al. 2004; Sazonov et al. 2005), shocks (Tabor & Binney 1993; Binney & Tabor 1995), magnetohydrodynamic wave-mediated plasma heating by cosmic rays (Boehringer & Morfill 1988; Rosner & Tucker 1989; Loewenstein et al. 1991), and cosmic-ray bubbles produced by the central AGN (Churazov et al. 2001, 2002; Reynolds et al. 2002; Brüggen 2003; Reynolds et al. 2005), which can heat intracluster plasma by generating turbulence (Loewenstein & Fabian 1990; Churazov et al. 2004; Cattaneo & Teyssier 2007) and sound waves (Fabian et al. 2003a; Ruszkowski et al. 2004a,b) and by doing pdV work (Begelman 2001; Ruszkowski & Begelman 2002; Hoeft & Brüggen 2004).

Another way in which central AGNs may heat the intracluster medium (ICM) is by accelerating cosmic rays that mix with the intracluster plasma and cause the ICM to become convectively unstable. A steady-state, spherically symmetric model based on this idea was developed by Chandran & Maron (2004) and subsequently refined by Chandran (2005) and Chandran & Rasera (2007). In this model, a central supermassive black hole accretes hot intracluster plasma at the Bondi rate, and converts a small fraction of the accreted rest-mass energy into cosmic rays that are accelerated by shocks within some distance r_{source} of the center of the cluster. The resulting cosmic-ray pressure gradient leads to convection (see Chandran & Dennis (2006) and Dennis & Chandran (2008)), which in turn heats the thermal plasma in the cluster core by advecting internal energy inwards and allowing the cosmic rays to do pdV work on the thermal plasma. The model also includes thermal conduction and cosmic-ray diffusion (viscous dissipation turns out to be smaller than the other forms of convective heating at all radii) and assumes a steady state in which the net heating rate balances radiative cooling throughout the cluster. The model uses

mixing-length theory to describe convection and its effects on the ICM and predicts a self-consistent profile for the rms amplitude of the turbulent velocity. By adjusting a single parameter in the model (r_{source}), Chandran & Rasera (2007) were able to achieve a good match to the observed density and temperature profiles in a sample of eight clusters. In several of the clusters in this sample, compact cooling flows arise within the central few kpc of the clusters because the rate of radiative cooling peaks much more sharply near the cluster center than either the convective or conductive heating rates. At even smaller radii in these clusters, the cooling flow makes a transition to a Bondi flow, in a manner similar to that described by Quataert & Narayan (2000). The size of the central cooling flow plays a role in regulating the mass accretion rate within the central Bondi flow, as described by Chandran & Rasera (2007).

In this paper, we explore the connection between this AGN-driven-convection model and the observed properties of the iron abundance profiles of cooling-core clusters. While observations of non-cooling-flow clusters show a nearly constant abundance profile, cooling-core clusters show very peaked iron distributions (De Grandi & Molendi 2001). Observations of the relative abundances of oxygen, silicon and iron suggest that the production of iron in these abundance excesses is dominated by SNIa (and possibly winds) from the central brightest cluster galaxy (BCG) (Ettori et al. 2002; Matsushita et al. 2002; de Plaa et al. 2006). If cooling cores are preserved over a timescale longer than 5 Gyr (Böhringer et al. 2004), then the observed amounts of excess iron (of order $10^8 M_{\odot}$) within the cluster core are compatible with the amounts produced within the BCG by SNIa (Cappellaro et al. 1999) and stellar winds (Ciotti et al. 1991). However, the shape of these abundance profiles is still a mystery. The distribution of iron is much broader than the distribution of the stars that produce the metals, which indicates some additional processes are needed to transport the metals out of the BCG into the surrounding ICM (Rebusco et al. 2005).

Recently, Rebusco et al. (2005) developed an analytical model of metal injection by SNIa and diffusion by turbulent gas motions. They suggested that the dissipation of the same stochastic gas motions would produce the heating required

to solve the cooling-flow problem. Using this model, Rebusco et al. (2005, 2006); Graham et al. (2006) found that diffusion coefficients of order $10^{28} - 10^{29} \text{ cm}^2 \text{ s}^{-1}$ are required to match the abundance profiles of cooling-core clusters, while spatial scales $\sim 10 \text{ kpc}$ and velocities of the order of few 100 km.s^{-1} are needed to compensate the gas cooling.

Although these studies offered an explanation for the observed abundance profiles as well as a solution to the cooling-flow problem, they did not explain how the rms amplitude of the turbulent velocity, u , is determined, or how the dependence of u on the radial coordinate r is determined. On the other hand, the AGN-driven-convection model of Chandran & Rasera (2007) provides a physics-based theoretical framework for calculating $u(r)$. In this paper, we combine this model for intra-cluster turbulence with the model of metal injection of Rebusco et al. (2005) in order to understand the production and transport of metals in the ICM. We describe these models further in sections 2 and 3. In sections 4 and 5 we apply these models to a sample of eight clusters. We discuss the possible implications of our results for the variability of the AGN power during a cluster's lifetime in section 6, and summarize our conclusions in section 7.

2. Model of iron injection by SNIa and winds

From the relative abundance of O, Si and Fe, Ettori et al. (2002); Matsushita et al. (2002); de Plaa et al. (2006) have shown that SNIa dominate the iron enrichment in these abundance peaks. After removing the contribution from SNII thought to originate from the early formation of the BCG as well as the background abundance from other galaxies, the remaining central iron excess originates mainly from SNIa and stellar winds of the central BCG. Following the work of Böhringer et al. (2004); Rebusco et al. (2005, 2006), we estimate the contribution of SNIa as,

$$\left(\frac{d\rho_{Fe}}{dt}\right)_{SNIa} = 10^{-12} \left(\frac{sr}{\text{SNU}}\right) \left(\frac{\eta_{Fe}}{\text{M}_{\odot}}\right) \left(\frac{\rho_L}{\text{L}_{\odot}^{\text{B}} \text{ kpc}^{-3}}\right) \times \left(\frac{t}{t_H}\right)^{-k} \text{M}_{\odot} \cdot \text{yr}^{-1} \cdot \text{kpc}^{-3}, \quad (1)$$

with sr the present supernova rate in SNU (supernovae per century and per $10^{10} \text{ L}_{\odot}^{\text{B}}$), $\eta_{Fe} = 0.7 \text{ M}_{\odot}$ the iron yield per SNIa, ρ_L the blue luminosity density, t the cosmic time, $t_H = 13.45 \text{ Gyr}$ the current age of the universe and k the exponent which describes how the supernovae rate increased in the past. The wind contribution is taken from Ciotti et al. (1991); Rebusco et al. (2005),

$$\left(\frac{d\rho_{Fe}}{dt}\right)_{winds} = \gamma_{Fe} \left(\frac{\dot{m}_{wind}}{\text{M}_{\odot} \cdot \text{yr}^{-1} \cdot \text{L}_{\odot}^{\text{B}-1}}\right) \left(\frac{\rho_L}{\text{L}_{\odot}^{\text{B}} \text{ kpc}^{-3}}\right) \times \left(\frac{t}{t_H}\right)^{-\alpha} \text{M}_{\odot} \cdot \text{yr}^{-1} \cdot \text{kpc}^{-3}, \quad (2)$$

with $\gamma_{Fe} = 2.8 \times 10^{-3}$ the mean iron mass fraction in the stellar winds of an evolved population, $\dot{m}_{wind} = 2.5 \times 10^{-11} \text{ M}_{\odot} \cdot \text{yr}^{-1} \cdot \text{L}_{\odot}^{\text{B}-1}$ the present star mass loss rate of a $\simeq 10 \text{ Gyr}$ old population and, $\alpha = 1.3$ specifying the time evolution of the star mass loss rate. The hidden parameter here is t_{age} , which is the age of the BCG. Eq.1 and Eq.2 are indeed only valid from $t_H - t_{age}$ to t_H . Before the formation of the galaxy, the production of metals is of course assumed to be null. We assume a Hernquist (1990) profile typical of elliptical galaxies,

$$\rho_L(r) = \frac{L_B}{2\pi} \frac{a}{r(a+r)^3}, \quad (3)$$

where $a = r_e/1.8153$ and r_e is the effective radius containing half of the projected luminosity.

We constrain the parameters sr , k and t_{age} so that the total observed amount of iron M_{Fe} equals to the total amount of iron from the model inside the radius corresponding to the last bin of the abundance observations (located at a radius r_b). Using this normalization procedure makes the resulting abundance profile quite insensitive to the particular values of our poorly known parameters because the only important ingredient for our purpose is the light profile. For example, varying k between 0 and 2 changes the final abundance by only a few percent (with the diffusion coefficients suggested by Rebusco et al. (2005, 2006); Graham et al. (2006)). Renzini et al. (1993); Rebusco et al. (2006) suggest a value of k between 1 and 2, we pick a value of $k = \alpha$ (that is the time dependence SNIa iron injection and wind iron injection are the same). In this way, we

factorize the time dependence and adopt a new simple expression,

$$\begin{aligned} \frac{d\rho_{Fe}}{dt} &= 10^{-12} \times \left(\frac{sr_{eff}}{\text{SNU}} \right) \left(\frac{\eta_{Fe}}{M_{\odot}} \right) \left(\frac{\rho_L}{L_{\odot}^B \cdot \text{kpc}^{-3}} \right) \\ &\times \left(\frac{t}{t_H} \right)^{-\alpha} M_{\odot} \cdot \text{yr}^{-1} \cdot \text{kpc}^{-3}, \end{aligned} \quad (4)$$

with $\alpha = 1.3$ and sr_{eff} an effective supernovae rate which includes the wind contribution. This effective supernovae rate will be determined directly from the observed mass of iron and is no longer a free parameter. The advantage of using Eq.4 is that our problem of metal production and transport depend now linearly on sr_{eff} . We therefore don't need to run our solver for the transport equation multiple times to get the right sr . Instead, we run our solver once and then adjust the value of sr_{eff} afterwards (thereby multiplying the abundance profile by a constant) to match the total observed iron mass.

The last parameter is the age of the BCG, which affects our results to some degree since an older galaxy allows more time for iron production and diffusion. A typical galaxy age is given by the stellar population of the BCG of order $\simeq 8 - 12$ Gyr (Jimenez et al. 2007). We adopt a fixed age in this range for all our clusters of 9 Gyr. The metal enrichment model is now entirely determined by the observational data L_B , r_e , M_{Fe} .

3. Diffusion of metals by AGN driven convection

We assume that there is steady-state convection in the ICM as described by the AGN-driven convection model of Chandran & Rasera (2007). Metals in the ICM are then advected as a passive scalar by the turbulent flow. The advection equation for the transport of metals is given by,

$$\frac{\partial \rho a}{\partial t} = -\nabla \cdot (\rho \mathbf{v} a) + \frac{d\rho_{Fe}}{dt}, \quad (5)$$

with ρ the gas mass density, a the mass fraction of iron, and \mathbf{v} the velocity field given by the AGN-driven convection model. Using mixing length theory and assuming spherical symmetry and a statistical steady state, we average equation (5) to

obtain the equation

$$\begin{aligned} \frac{\partial \langle \rho \rangle \langle a \rangle}{\partial t} &= \frac{\dot{M}}{4\pi r^2} \frac{\partial \langle a \rangle}{\partial r} + \langle \frac{d\rho_{Fe}}{dt} \rangle \\ &+ \frac{1}{r^2} \frac{\partial}{\partial r} \left[r^2 D \langle \rho \rangle \frac{\partial \langle a \rangle}{\partial r} \right], \end{aligned} \quad (6)$$

where $\langle \dots \rangle$ indicates an ensemble average, \dot{M} is the mass accretion rate which is independent of the radius and is equal to the Bondi rate near the center (at $r \approx 0.2$ kpc), $\langle \frac{d\rho_{Fe}}{dt} \rangle \approx \frac{d\rho_{Fe}}{dt}$ is the above metal production rate from Eq.4, $\langle \rho \rangle = \rho$ is the gas density, $\langle a \rangle = a$ is the mass fraction of iron,

$$D = 0.5 l u_{NL} \quad (7)$$

is the diffusion coefficient, $l = 0.4r$ is the mixing length, and u_{NL} is the radial component of the turbulent velocity from the mixing-length-theory-based AGN-driven convection model, as calculated by Chandran & Rasera (2007). The factors 0.5 and 0.4 are chosen to be consistent with the value used by Chandran & Rasera (2007) for the different energy fluxes. The factor of 0.5 in equation (7) is much larger than the numerical coefficient in Equation 8 of Dennis & Chandran (2005), which reads $D_{\text{eddy}} = 0.11UL\xi$. However, in this last equation, U is the rms value of the full velocity vector, not just its radial component. Similarly, L is the full correlation length of the turbulence, whereas the mixing length l is just the radial component of the typical displacement of a fluid element before it is mixed into the surrounding fluid. (The quantity ξ accounts for the possible reduction in D_{eddy} if the motions are oscillatory and only weakly turbulent.) If one sets $u \simeq U/\sqrt{3}$ and $l \simeq L/\sqrt{3}$, then $D = 0.167LU$ in equation (7), which is similar to equation 8 of Dennis & Chandran (2005). It should also be noted that if we were to choose a smaller numerical constant in equation (7) and throughout the mixing-length model of Chandran & Rasera (2007), the resulting turbulent velocities in the model would become larger so that the energy fluxes and convective heating were still able to compensate for radiative cooling. The resulting value of D would not be greatly altered, since it is closely tied to the rate of convective heating, which is fixed in the AGN-convection model by the requirement that heating balance cooling in steady state.

The evolution of the abundance depends on two terms. The first term is related to the accretion rate \dot{M} and corresponds to an inward advection of the abundance profile at a speed $v_{\dot{M}}(r) = \dot{M}/(4\pi r^2 \rho)$. If we were to assume a large accretion rate as in the cooling-flow model (e.g., $\dot{M} = 100 - 1000 \text{ M}_{\odot} \text{ yr}^{-1}$) the accretion of low-abundance gas from larger radius would destroy the central abundance excess (Böhringer et al. 2004). However, in the AGN-driven convection model, $\dot{M} \lesssim 1 \text{ M}_{\odot} \text{ yr}^{-1}$, and the effect of inflow is small except within the central few kpc, where the $1/(\rho r^2)$ dependence of $v_{\dot{M}}(r)$ causes $v_{\dot{M}}$ to become large. The second term corresponds to diffusion resulting from the random turbulent velocity field. This term dominates and smoothes the abundance profile on a scale $r \approx 58 \times [(D/10^{29} \text{ cm}^2 \text{ s}^{-1}) \times (t_{\text{age}}/10 \text{ Gyr})]^{0.5} \text{ kpc}$, which is comparable to the typical half-mass radius of the central iron excesses.

We have solved Eq.6 taking a null initial abundance and assuming a null second derivative of the iron abundance profile for the boundary conditions. The discretization of the advection part doesn't require any artificial diffusion since the physical diffusion dominates for our case. We have run our code to compute the iron abundance profile of 8 cooling-core clusters.

4. Properties of the sample of 8 cooling-core clusters

Our sample consists of 8 cooling-core clusters for which we have the turbulent velocity profile from the AGN-driven convection model (Chandran & Rasera 2007): Virgo, Abell 262, Sersic 159-03, Abell 4059, Hydra A, Abell 496, Abell 1795 and Perseus. The redshifts of these clusters are taken from Kaastra et al. (2004). The properties of these clusters and their brightest cluster galaxies (BCGs) are summarized in table 1 and table 2. We use the current Λ CDM cosmology ($H_0 = 70 \text{ km.s}^{-1} \text{ Mpc}^{-1}$, $\Omega_m = 0.3$ and $\Omega_{\Lambda} = 0.7$).

4.1. Photometric properties

The photometric properties we are interested in are the total luminosity L_B , and the effective radius r_e , which contains half of the projected flux. We get the name of the brightest cluster galaxies

(BCG) in each cluster from Rafferty et al. (2006) and the NED database, and then compute the total blue luminosity using the Hyperleda database (Paturel et al. 2003) proceeding as follows. We take the apparent corrected blue magnitude of the BCGs, compute the luminosity distance, and the associated distance modulus from our redshift and the Λ CDM cosmology. We finally compute the blue absolute magnitude, and the blue luminosity assuming $M_{\odot}^B = 5.47$.

Finding the effective radius is more challenging. We use three different sources: Schombert (1987) (Perseus, Abell 1795, and Virgo), Graham et al. (1996) (Abell 262 and Abell 496) and Hyperleda (Hydra A, Sersic 159-03, and Abell 4059). In these references an $R^{1/4}$ law (de Vaucouleurs 1953) is adjusted to the observed profile from which the best fit effective radius (or the effective surface brightness in Hyperleda) is deduced. We also convert to our cosmology using the ratio of angular diameter distance for our cosmology and redshift to the angular diameter distance for the authors' cosmology and redshifts. The results for r_e and L_{cr} are shown in table 1.

We note that we neglect the cores observed on small scales (Carollo et al. 1997), the deviation from the $R^{1/4}$ law (Graham et al. 1996) on intermediate scale, the large envelopes observed on large scales (Schombert 1988) and the ellipticity of the profiles. We do not hide here that the uncertainties on r_e and L_B are important. Fortunately, the result on the shape doesn't depend on L_B (due to our renormalization procedure) and has only a little dependency on r_e for most of the clusters because the diffusion scale is larger than r_e .

4.2. Gas density and turbulent velocity profile

We take the eight clusters in our sample to have the density profiles and (as discussed above) turbulent-velocity profiles obtained from the AGN-driven convection model of Chandran & Rasera (2007). The model density profiles are very similar to the observations of Kaastra et al. (2004), as shown in Figure 1 of Chandran & Rasera (2007). We note that the AGN-driven-convection-model solutions were obtained by varying the size of the cosmic-ray acceleration region in the model in order to achieve a best-fit to the observed density

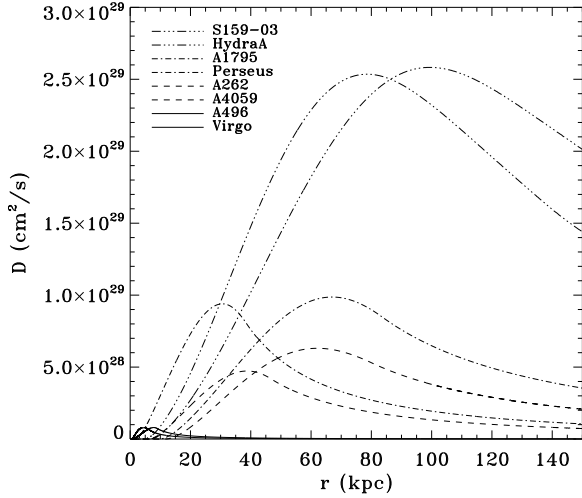


Fig. 1.— Diffusion coefficient (due to the stochastic turbulent motions of the gas) for our 8 clusters. This comes from the AGN-driven convection model of Chandran & Rasera (2007).

and temperature profiles of the eight clusters in our sample. The model solutions were therefore not fine-tuned to solve the independent problem we are investigating now; the shapes of the abundance profiles. From the turbulent radial velocity profile u_{NL} , we deduce the diffusion coefficient of Eq.6, $D(r) = 0.2r \times u_{NL}$.

The profiles of the diffusion coefficients are presented in Fig.1. The diffusion coefficients peak around a radius r_{max} where the diffusion reaches its maximum D_{max} . We divide the clusters into 4 levels of diffusion. Virgo and Abell 496 have the smallest diffusion coefficients, with $D_{max} \approx 8 \times 10^{27} \text{cm}^2 \cdot \text{s}^{-1}$. They are the “very weak feedback clusters”. Abell 4059 and Abell 262 have small diffusion coefficients ($D_{max} \approx 5 \times 10^{28} \text{cm}^2 \cdot \text{s}^{-1}$) and are called “weak-feedback clusters”. Perseus and Abell 1795 have intermediate diffusion coefficients ($D_{max} \approx 10^{29} \text{cm}^2 \cdot \text{s}^{-1}$) and are called “moderate feedback clusters”. Finally, Hydra A and Sersic 159-03 have large diffusion coefficients ($D_{max} \approx 2.5 \times 10^{29} \text{cm}^2 \cdot \text{s}^{-1}$) and are the “strong-feedback clusters”. We summarize the value of D_{max} and r_{max} in table 2.

4.3. Observed abundance profiles

We find the observed abundance profiles in the literature (helped in this way by the BAX clus-

ter database (Sadat et al. 2004)). All the data points come either from Chandra or XMM observations. We converted all the radii to kpc using the angular diameter distance from Λ CDM cosmology. Finally, we converted all the different solar abundances to the value published by Anders & Grevesse (1989) (where the solar abundance relative to H is 4.68×10^{-5} in number). The references used are the following: Virgo (Matsushita et al. 2002), Abell 262 (Vikhlinin et al. 2005), Sersic 159-03 (de Plaa et al. 2006), Abell 4059 (Choi et al. 2004), Hydra A (David et al. 2001), Abell 496 (Tamura et al. 2001a), Abell 1795 (Ettori et al. 2002), and Perseus (Churazov et al. 2003). We include all the observational points with two exceptions. We neglect the abundance hole observed within the central several kpc in Perseus (3 points at $r < 10$ kpc), Abell 262 (3 points are $r < 10$ kpc) and Virgo (1 point $r < 1$ kpc). In the case of Perseus, Churazov et al. (2003) mentions that the profile may be affected by the bright compact source in this region. We also removed the data points that suddenly drop to very low values at large r (the last point in the case of Sersic 159-03 and two last points in the case of Abell 262). We also note that we used the deprojected profiles for clusters Perseus, Virgo, Abell 496 and Abell 4059 and projected profiles for clusters Hydra A, Sersic 159-03, Abell 262 and Abell 1795 because deprojected profiles were not available. We do not expect this to have a large effect on our conclusions, because for the cases for which we have both projected and deprojected profiles, the two types of profile are similar, with the main difference being that the deprojected profile is more noisy. The resulting abundance profiles are shown in Fig.2.

This figure shows that the ranges of values for the abundance profiles are relatively similar. We note that the normalization of the abundance profile of Sersic 159-03 is lower than the others. This lower normalization may be related to the soft X-ray excess, which is most likely of non-thermal origin (Werner et al. 2007) and may contribute to the continuum. For $r < 100$ kpc a central abundance peak is observed for all eight clusters while at larger radii (100 – 300 kpc), the profiles flatten and reach an asymptotic value of $a \sim 0.2 - 0.4$. This similar shape for all the clusters may indicate a common mechanism for creating the abundance

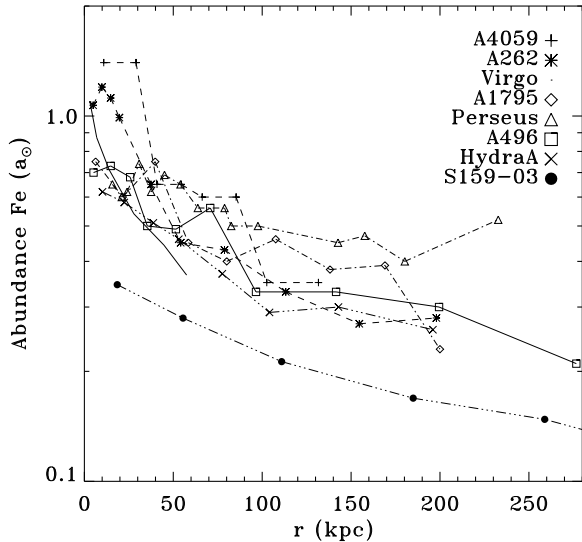


Fig. 2.— Observed abundance profiles in solar unit for our 8 clusters (Chandra or XMM). We decompose them into a central iron excess from the BCG ($r < 100$ kpc) and an asymptotic abundance from the background galaxies ($r > 100$ kpc).

profiles and allows us to decompose the profiles in two parts: a flat contribution and a central excess. We note that three out of the four highest peaks (Virgo, Abell 4059 and Abell 262) correspond to the clusters with less diffusion (see Fig.1 in our model).

Following the work of Böhringer et al. (2004); Rebusco et al. (2005, 2006), we subtract a constant value a_b from the observed abundance profiles. a_b corresponds to the contribution of iron from the background galaxies as well from SNII. Our goal is to isolate the central iron excess or more precisely the iron contribution from the BCG itself. Indeed, De Grandi & Molendi (2001) measured the abundance profiles at large radii for 17 clusters. They showed that the abundance profiles of all non-cooling-core clusters are consistent with being constant with radius at a value of order 0.2-0.4. On the other hand, cooling-core clusters present a peak near the center and an asymptotic value at large radii at the same value of order 0.2-0.4. Moreover, an analysis of the elemental abundance pattern in M87 (Finoguenov et al. 2002) and Sersic 159-03 (de Plaa et al. 2006) has shown that SNIa dominate the metal enrichment in the central region and that their contribution decreases with

radius. These observations support the idea of a background value from SNII in galaxies throughout the cluster.

To estimate these background values a_b , we take the average values of the last three points in the vicinity of 100 kpc. Then, to avoid negative abundances, we remove the points where $a < a_b$. Since the observations of Virgo do not reach 100 kpc and seems to be below the other curves at intermediate radii, we choose a typical value $a_b = 0.2$. The last observational points are located at a distance r_b from the center. The values of a_b and r_b are shown in table 2.

From the density profile and the abundance profile, we deduce the total observed mass of iron in the central excess M_{Fe} (see table 1). This mass is the mass of iron inside r_b . In our model, we always choose sr_{eff} so that the mass of iron inside r_b is also equal to M_{Fe} . We also characterize the width of the abundance profile by computing $r_{1/2}$, the radius which contains half the total observed mass of iron in the central excess (inside r_b).

5. Impact of present AGN-driven convection on iron distribution

Using the model described in sections 2 and 3 and the parameters from section 4, we compute numerically the iron abundance profiles for the eight clusters in our sample and compare to observations. For the sake of comparison, we first compute the abundance profile without any diffusion or inflow velocity. The result is shown as a dashed line in Fig.3 and Fig.4. Clearly, such profiles are too steep near the center and do not match the observations (diamonds). These profiles basically show that the observed distributions of iron do not follow the distributions of stars within the BCG galaxies. This is because the effective radii of the luminosity distribution r_e (table 1) are smaller than the observed half iron mass radii $r_{1/2}$ (table 2).

Taking into account the diffusion and the inflow velocity brings the model profiles substantially closer to the observations. This is illustrated by the continuous lines in Fig.3 and Fig.4. Interestingly, we find the same classification as in subsection 4.2 when studying the intensity of the diffusion coefficient. In the very “weak feedback clusters” with the least diffusion (Virgo and Abell

496), abundances are largely overestimated in the inner 20 kpc by a factor larger than four and underestimated at $r > 50$ kpc. “Very weak feedback clusters” do not have enough present convection to diffuse the iron to larger radii. In the “weak feedback clusters” with little convection (Abell 4059 and Abell 262), abundances are underestimated near 30 kpc by a reasonable factor of 1.5-2. The “moderate feedback clusters” with intermediate diffusion coefficients (Perseus and Abell 1795) provide a much better agreement with the observed abundance profiles. Their present convection is almost enough to shape the abundance profiles so that they are compatible with the observational points. Finally, in the “strong feedback clusters” (Sersic 159-03 and Hydra A), the diffusion coefficients are sufficiently large or even too large and the abundance near the center is compatible (Sersic 159-03) or even too small by a factor of ~ 2 in the inner 70 kpc (Hydra A). We draw the conclusion that turbulence at the level predicted by the AGN-driven convection model cannot be neglected when considering the iron distribution in “moderate” or “strong feedback clusters”.

If AGN-driven convection is the dominant mechanism for transporting metals, our iron abundance profile plots in Fig.3 and Fig.4 suggest that Virgo-like clusters with low present convection require a lot more convection in the past to match observations whereas Hydra A-like clusters with a lot of present convection require less past convection to match observations. This coincides with the natural idea that clusters and more specifically their central AGN were not in their current state during all their history (Pope 2007), an idea that we investigate more thoroughly in the next section.

6. Insight into the past variations of the AGN power from the shape of the abundance profiles

Pope et al. (2006) suggested that clusters are heated by Hydra-A type events interspersed between epochs of lower AGN power. In this section we explore this idea and the more general possibility that the AGN power varies in some fashion during the lifetime of a cluster. As a consequence of this variation, the amplitude of the AGN-driven convection will also evolve. Ideally, to investigate

the effects of a time-varying diffusion coefficient on the present-day abundance profile, we would solve equation (6) using the correct individual history of convection for each cluster in our sample. However, we have no reliable way of determining these individual histories. Instead, we adopt the following approach. First, we develop a model for relating the turbulent velocity profile in a cluster directly to its AGN power (Sect.6.1). Second, for each cluster in our sample, we determine the constant AGN power that would be needed in order for the resulting turbulent velocity profile to bring the iron abundance profile into agreement with observations. We then take this constant AGN power to be a proxy for the time-averaged AGN power within the cluster over the last ~ 10 Gyr. In following this procedure, we make the strong hypothesis that the AGN-driven convection is the only physical process that transports iron in the ICM.

One way of thinking about the cause of the varying accretion rate of the central AGN is provided by the same AGN-driven convection model of Chandran & Rasia (2007) that we have been using to model the turbulent velocity profile. In this model, the value of the AGN power (which we take to be comparable to L_{cr}) is determined primarily by two factors: the density ρ_{core} and temperature T_{core} of the intracluster plasma at the radius $r_{\text{core}} \simeq 50 - 100$ kpc. These parameters provide the outer boundary conditions for the strongly cooling cluster core. For larger ρ_{core} , the rate of radiative cooling within r_{core} is larger, and thus more heating is needed to balance cooling, leading to a larger value of L_{cr} . (In a time-dependent model, if cooling were to initially exceed the total heating, then the plasma would cool and flow inward, causing the AGN mass accretion rate to grow until a balance between heating and cooling is reached.) Similarly, for a smaller T_{core} , the conductive heating becomes smaller (the conductivity being $\propto T^{5/2}$) and more convective heating is needed in order for total heating to balance cooling. In the AGN-driven convection model, small variations in ρ_{core} and T_{core} cause large variations in the AGN power. The value of L_{cr} will thus evolve as ρ_{core} and T_{core} change in time due to, e.g., mergers, streams of infalling baryons, and stripping of gas from cluster galaxies.

6.1. Analytical fit of the convection profile depending on the AGN power only

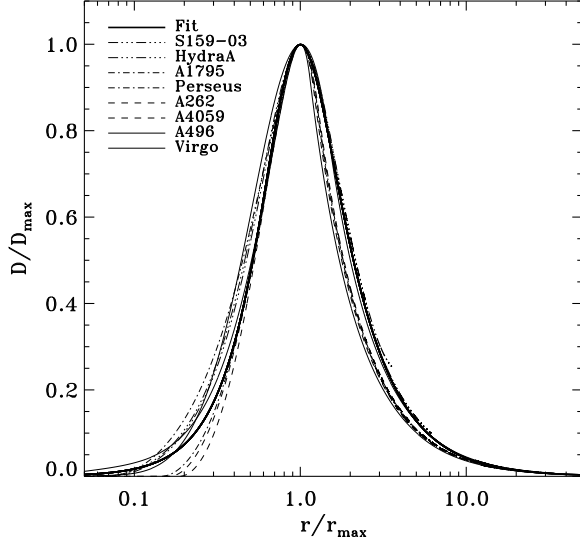


Fig. 5.— Diffusion coefficient (deduced from turbulent velocity field) normalized to its maximal value as a function of the radius normalized to the radius where the diffusion coefficient is maximum. The dashed lines are for our 8 clusters. Their profiles are self-similar. The thick continuous line is the fit given by Eq.8.

In Fig.5 we plot D/D_{\max} as a function of r/r_{\max} for the eight clusters in our sample, where r_{\max} is the radius at which D achieves its maximum. The shapes of the different curves are similar, and so we are able to obtain a reasonable fit to the diffusion coefficients using the analytic function

$$\frac{D(r)}{D_{\max}} = 1.88 \times \left[1 + \left(\frac{0.934 r_{\max}}{r} \right)^4 \right]^{-0.525} \times \left[1 + \left(\frac{r}{0.934 r_{\max}} \right)^4 \right]^{-0.4}. \quad (8)$$

The result of this fitting procedure is shown as a solid thick line in Fig.5. For $r \gg r_{\max}$ the right-hand side of equation (8) scales like $r^{-1.6}$ whereas for $r \ll r_{\max}$ it scales like $r^{2.1}$. Equation (8) matches the diffusion coefficient at $r > 0.2 r_{\max}$ fairly well. For smaller radii, Eq.8 is still compatible but the diffusion coefficient from the model drops more strongly for some clusters.

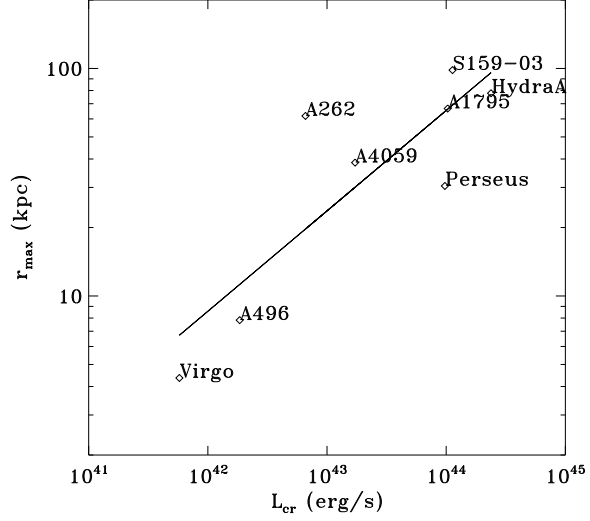


Fig. 6.— Correlation between the radius where the diffusion is maximum and the cosmic-ray luminosity. Right: Correlation between the maximum of the diffusion coefficient and the cosmic-ray luminosity.

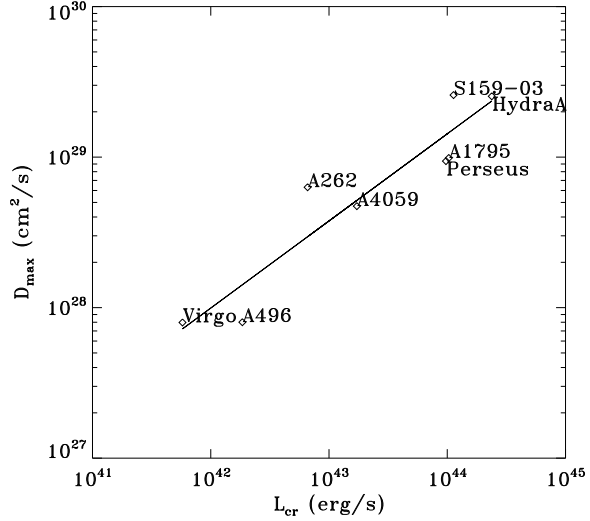


Fig. 7.— Correlation between the maximum of the diffusion coefficient and the cosmic-ray luminosity.

To develop a simpler one-parameter fit for $D(r)$, we note that the quantities D_{\max} and r_{\max} are closely correlated to the cosmic-ray luminosity L_{cr} of the central AGN in the AGN-driven convection model. These correlations are shown in Fig.6, Fig.7, and allow us to express D_{\max} and r_{\max} in

terms of L_{cr} using the best-fit power-law relations:

$$r_{max} = 3.1 \times \left(\frac{L_{cr}}{10^{41} \text{ erg.s}^{-1}} \right)^{0.44} \text{ kpc.} \quad (9)$$

$$D_{max} = 2.6 \cdot 10^{27} \left(\frac{L_{cr}}{10^{41} \text{ erg.s}^{-1}} \right)^{0.58} \text{ cm}^2 \cdot \text{s}^{-1} \quad (10)$$

The correlation between D_{max} and L_{cr} results from the fact that the convection is triggered by the gradient of cosmic-ray pressure; thus, more cosmic-ray energy injection will increase the convection level and the resulting diffusion. We note that L_{cr} is not a free parameter of the AGN-driven convection model, but rather is determined self-consistently within the model so that the resulting convective heating (which increases with increasing L_{cr}) is sufficiently large that the total heating (convective plus conductive) balances radiative cooling.

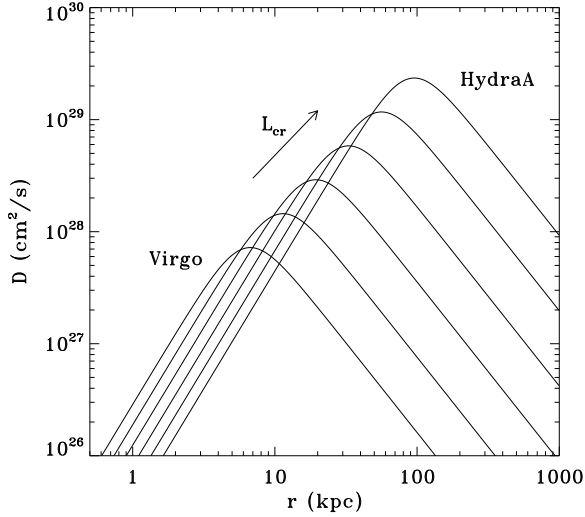


Fig. 8.— Diffusion coefficient profile (due to AGN-driven convection) as a function of the radius for different cosmic-ray luminosities (AGN power). The cosmic-ray luminosities increases from $5.8 \times 10^{41} \text{ erg.s}^{-1}$ (Virgo on the left) to $2.4 \times 10^{44} \text{ erg.s}^{-1}$ (Hydra A on the right) by a factor of 3.33 each time. This comes from the analytical fit Eq.8 and is used to determine which time average AGN power is required to match the observed abundance profiles.

The accuracy of the analytical fit is of course degraded when we use equations (9) and (10) in equation (8), since we have decreased the number

of parameters. However, we have now achieved a reasonable fit of the diffusion profile (due to AGN-driven convection) depending only on L_{cr} (the cosmic-ray luminosity or AGN power). The evolution of the profile as a function of L_{cr} is shown Fig.8 where the cosmic ray luminosity is increased from Virgo's value ($L_{cr} = 5.8 \times 10^{41} \text{ erg.s}^{-1}$) to the Hydra A's value ($L_{cr} = 2.4 \times 10^{44} \text{ erg.s}^{-1}$) by a factor 3.33 each time.

The diffusion term in Eq.6 can therefore be expressed as a function of the cosmic-ray luminosity. We note that the inflow term in Eq.6 can also be evaluated from the cosmic-ray luminosity since the accretion rate is given by

$$\dot{M} = \frac{L_{cr}}{0.005 \times c^2}. \quad (11)$$

We have taken here the efficiency from Chandran & Rasera (2007). This accretion rate will be useful to solve Eq.6 in the next part.

6.2. AGN power required to match the abundance profile

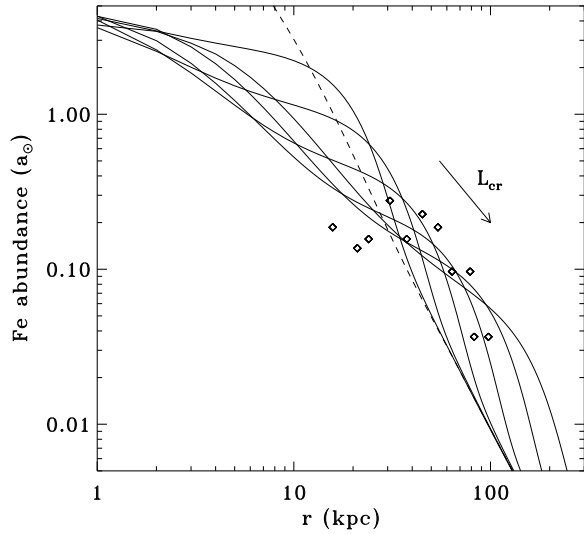


Fig. 9.— Perseus abundance profile as a function of the radius for different cosmic-ray luminosities (AGN power). The cosmic-ray luminosities increases from $5.8 \times 10^{41} \text{ erg.s}^{-1}$ (Virgo on the middle top) to $2.4 \times 10^{44} \text{ erg.s}^{-1}$ (Hydra A on the bottom right) by a factor of 3.33 each time. It shows that by varying L_{cr} we can reasonably match the abundance profile.

We now solve our model using the convection profile as given by Eq.8 (for the diffusion term) and the accretion rate as given by Eq.11 (for the inflow term). The only free parameter is the AGN power. We show in Fig.9 the evolution of the abundance profile as a function of the AGN power. We deduce the luminosity L_{cr}^{fit} which provides the best fit to the abundance profile. The resulting profiles are presented in Fig.3 and Fig.4 as a dashed-dotted line. The first conclusion is that we obtain a good match for all the profiles by varying this single free parameter. This was not obvious because we cannot adjust the size and the normalization of the diffusion coefficient independently. Moreover, the diffusion drops by a factor 10 outside of the region $0.2r_{max} < r < 5r_{max}$ and has very little effect outside this region. The position of the peak of diffusion exactly where we need diffusion to explain the abundance profile is a striking coincidence. It means that by choosing the right AGN power one could reproduce the shape of the observed iron excesses. We also compute the half iron mass radius $r_{1/2}^{fit}$ for each cluster (table 3). This is the radius which contains half the total iron mass of the model inside r_b (distance to the center of the last observational point). The reasonable agreement with the observed half iron mass radius $r_{1/2}$ (table 2) computed inside the same radius r_b confirms the above conclusion.

The following question naturally arises: are these average cosmic-ray luminosities (L_{cr}^{fit}) realistic? Nothing guarantees realistic values in our fitting process. The question is particularly interesting for the “very-weak feedback clusters” such as Virgo and Abell 262, and the “strong feedback cluster” Hydra A, which do not fit the observed abundance profiles with the present convection.

The best-fit values of the cosmic-ray luminosity L_{cr}^{fit} are summarized in table 3 and can be compared with the present cosmic-ray luminosity L_{cr} in table 1. Also shown in table 3 is the maximum of the diffusion coefficient D_{max}^{fit} , and its radius r_{max}^{fit} , which can be compared with the present value r_{max} and D_{max} in table 2. We recover here the same kind of value for the diffusion coefficient value $D_{max}^{fit} = 10^{28} - 10^{29} \text{ cm}^2.\text{s}^{-1}$ (equivalent to maximum rms turbulent velocities between 70 and 110 km.s^{-1}) as Rebusco et al. (2005, 2006); Graham et al. (2006). The advantage in our approach is that the shape of the diffusion coefficient

comes from the physics-based AGN-driven model of Chandran & Rasia (2007) and that we are also able to derive the corresponding cosmic-ray luminosities.

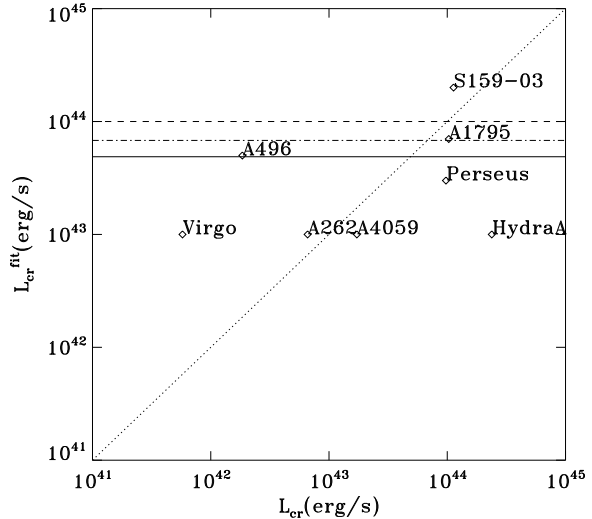


Fig. 10.— AGN power (cosmic-ray luminosity L_{cr}^{fit}) required to match the abundance profile as a function of the present AGN power (cosmic-ray luminosity L_{cr}) for our 8 clusters. The dotted line shows the equality between these two quantities. On this line, convection at present level sustained during the past 10 Gyr would be enough to explain the distribution of metals. The continuous line is the average $\langle L_{cr}^{fit} \rangle = 4.9 \times 10^{43} \text{ erg.s}^{-1}$ over all the clusters. The dashed line is the estimate from Voit & Donahue (2005) using entropy-floor observations and the dot-dashed line is an estimate from Best et al. (2007) using radio observations. The proximity of these values to our average suggests an alternation of Virgo-type feedback, Perseus-type feedback, and Hydra-A type feedback and could explain the distribution of metals in clusters of galaxies.

Fig.10 shows the average cosmic-ray luminosities L_{cr}^{fit} as a function of the present cosmic-ray luminosity L_{cr} . The dotted line shows the equality between these two quantities. Clusters located near this diagonal line have about the right amount of present convection to explain the shape of the iron distribution (if this convection was sustained during the past 10 Gyr). We recover the previously mentioned result that Hydra A has too much convection whereas Virgo and

A496 have too little (and the other clusters have approximatively the right amount of present convection). What is interesting is that the average $\langle L_{cr}^{fit} \rangle = 5 \times 10^{43} \text{ erg.s}^{-1}$ is about the same as the average of the present cosmic-ray luminosities $\langle L_{cr} \rangle = 7 \times 10^{43} \text{ erg.s}^{-1}$. Moreover, the dispersion of cosmic-ray luminosities is much less since $L_{cr}^{fit} = 10^{43} - 10^{44} \text{ erg.s}^{-1}$ whereas $L_{cr} = 10^{41} - 10^{44} \text{ erg.s}^{-1}$. This is exactly what we would expect if in the cluster history the cosmic-ray luminosities evolved randomly between Virgo values, Perseus values and Hydra-A values. The average over all the clusters would be conserved and the dispersion of cosmic-ray luminosities would decrease.

We have searched the literature to find other constraints on the average cosmic-ray luminosities in order to check if such values are realistic. Direct measurement of the convection profile is, of course, out of reach. The better constraints come from feedback considerations. A study by Pope et al. (2006) of the heating rate of cooling-core clusters suggests an alternation between Hydra-A type events and smaller-scale outflows. By studying the entropy floor in cooling-core clusters with and without radio emission, Voit & Donahue (2005); Donahue et al. (2006) suggest also an episodic heating. The invoked values are $10^{45} \text{ erg.s}^{-1}$ for 10^7 yr once every 10^8 yr . This leads to an average of $10^{44} \text{ erg.s}^{-1}$, which is comparable to our value given the uncertainties.

The average of the observational estimates of the present mechanical luminosities in a large sample of clusters could also provide a rough estimate of the temporal average of the AGN power (although the accuracy of such an estimate is reduced by its failure to take into account evolution with redshift). Birzan et al. (2004); Rafferty et al. (2006) obtain a sample of 33 cooling-core clusters with measured mechanical luminosities. The values range from $10^{42} \text{ erg.s}^{-1}$ to $10^{46} \text{ erg.s}^{-1}$ with an average of $9 \times 10^{44} \text{ erg.s}^{-1}$ but we note that the sample is certainly biased towards the high rate for $z > 0.1$. If we remove these clusters, the average falls to $2 \times 10^{44} \text{ erg.s}^{-1}$. These samples contain only a small number of clusters because of the difficulty of detecting X-ray cavities and measuring their properties.

Another approach was taken by Best et al. (2007) who measured the radio luminosities for the BCG of 625 nearby groups and clusters. Using the conversion between mechanical luminosity and radio-luminosity from Birzan et al. (2004); Rafferty et al. (2006), they converted the radio luminosity function into a mechanical luminosity function. The average over the sample of BCG provides an estimate of the time-averaged mechanical luminosities, $\langle L_{mech} \rangle = 2.3 \times 10^{42} f(M_*/10^{11} M_\odot) \text{ erg.s}^{-1}$, with f their uncertainty factor, and M_* the stellar mass. Assuming a stellar mass to blue light ratio of 5.3 (Borriello et al. 2003), the average of our stellar masses is $7.4 \times 10^{11} M_\odot$. A factor $f = 1$ would mean that an energy of 1 *PV* is considered per bubble. If we take $f = \gamma/(\gamma - 1) = 4$, as in Best et al. (2007), then we obtain an average mechanical power of $\langle L_{mech} \rangle = 6.8 \times 10^{43} \text{ erg.s}^{-1}$, which is in good agreement with our estimate using the iron distribution.

Another constraint comes from the mass of the central black hole, which equals the time integral of the mass accretion rate (plus a tiny contribution from the initial black hole seed plus a possible contribution from black-hole mergers). Since the central black hole may have grown substantially before the formation of the cluster, the present value of the black hole mass provides only an upper bound on the average mass accretion rate of the black hole during the lifetime of the cluster. Assuming a black hole of mass $3 \times 10^9 M_\odot$ (as in Virgo), the average accretion rate must be smaller than $0.3 M_\odot.\text{yr}^{-1}$. This accretion rate corresponds to an average cosmic-ray luminosity of $1.9 \times 10^{45} (\eta/0.1) \text{ erg.s}^{-1}$, where η is the efficiency with which the central AGN converts the rest mass energy of accreted plasma into cosmic-ray luminosity (which we take to be comparable to the total AGN power). Allen et al. (2006) suggest that roughly 2.2 % of the Bondi accretion power is transformed into AGN mechanical luminosity. Using this value for η , we find that the cosmic-ray luminosity must be less than roughly $4.1 \times 10^{44} \text{ erg.s}^{-1}$, which is larger than our value. Moreover, it should be noted that the Bondi accretion rate may significantly exceed the rate at which mass accretes onto the central black hole, since much of the accreting plasma may end up form-

ing stars (Tan & Blackman 2005) or being ejected in an outflow (Blandford et al. 1999). We thus conclude that our average value of L_{cr}^{fit} is compatible with present-day black hole masses. Cosmological simulations from Sijacki et al. (2007); Di Matteo et al. (2007) also indicate black hole accretion rates and mechanical luminosities in the same range of values with large variations. In these simulations, the final black hole mass comes from mergers and accretion in high redshift quasar phases.

Our value of $L_{cr}^{fit} \sim 5 \times 10^{43} \text{ erg.s}^{-1}$ seems reasonable and compatible with current constraints (see Fig.10). If our scenario is correct, it indicates that the iron distribution could put strong constraints on the AGN feedback model. For instance, an average AGN power greater than $2.4 \times 10^{44} \text{ erg.s}^{-1}$ would destroy the observed abundance profile of most of the clusters as illustrated Fig.9. Moreover, our scenario gives further support for the idea that convection plays a fundamental role in clusters of galaxies by explaining the density and temperature profile as well as the shape of the iron abundance excess. Our model is, however, very simplistic and relies on many approximations. In order to be more realistic, one would have to carry out cosmological simulations with AGN feedback and supernovæ enrichment as Sijacki et al. (2007); Di Matteo et al. (2007). However, a proper treatment of the convection would also require the inclusion of cosmic rays and anisotropic transport (Rasera & Chandran 2007) since these two ingredients modify the convective instability criterion (Balbus 2000; Chandran & Dennis 2006; Dennis & Chandran 2008; Parrish & Quataert 2008; Quataert 2008).

7. Conclusion

In this article, we have studied the impact of AGN-driven convection on the shape of the iron abundance profile for 8 cooling-core clusters: Perseus, Hydra A, Sersic 159-03, Abell 262, Abell 1795, Virgo, Abell 496 and Abell 4059. We have used the iron injection model from Böhringer et al. (2004) where metal production by SNIa and winds follows the Hernquist light profile of the central brightest cluster galaxy (BCG).

We have also used the steady-state convection model from Chandran & Rasera (2007) to determine the turbulent velocity profile in the ICM. In this model, AGN-driven convection is the dominant mechanism for transferring energy from the central AGN to the ICM thereby preventing large quantities of plasma from cooling to low temperatures.

Stochastic motions with an rms radial velocity fluctuation u_{NL} correspond to a diffusion coefficient $D = 0.5lu_{NL}$ in the mixing length-theory employed by Chandran & Rasera (2007), where l is the mixing-length which we set to $0.4r$. We have solved a 1D advection-diffusion equation for the iron abundance profile, and compared our results to XMM and Chandra abundance profiles. The profiles obtained without diffusion (metal injection only) are too peaked toward the center. Taking into account AGN-driven convection improves the abundance profile because it smoothes the center. For most objects in our sample the modeled profiles do not differ greatly from the observations. However, the less convective clusters (Abell 496 and Virgo) require much more convection in order to match observations whereas the most convective cluster (Hydra A) requires less.

Making use of the approximate self-similarity of the diffusion coefficient profiles in the AGN-driven convection model, we model the diffusion coefficient as a function of radius r that depends only on one parameter, namely the cosmic-ray luminosity (AGN power). We have used this function to find if any reasonable AGN power could provide a good fit to the observed iron distributions. Although the diffusion coefficient is non-negligible only in a limited range of radii around its maximum, and although we cannot adjust the amplitude and the position of this maximum independently, we find a good match for all the clusters.

The best-fit AGN powers L_{cr}^{fit} can be thought as the time average over the cluster history (10 Gyr) required to explain entirely the width of the abundance profile. We found a range of values for L_{cr}^{fit} between 10^{43} and $2 \times 10^{44} \text{ erg.s}^{-1}$, with an average of $5 \times 10^{43} \text{ erg.s}^{-1}$. Such a value seems quite reasonable and compatible with current constraints on the entropy profile, black hole mass, and radio-

inferred average mechanical luminosity. The shape of the abundance profile could therefore be a fossil record of the past AGN-driven convection.

This model relies on several approximations. The separation of the abundance profile into a constant component a_b (from the background galaxies and SNII) and an iron excess (from the central BCG) is one of the major approximations. A better method would be to also include the contribution from other galaxies and SNII and to compare with the total abundance profile, however this contribution also suffers from a lot of uncertainties. We also neglect all other possible sources of convection such as supernova winds, the jet itself, and stirring by infalling galaxies. This may explain the discrepancy between our results and the observed abundances at the very centers of several of the clusters, in some of which an abundance hole is observed. Another step towards a more realistic model would be cluster simulations with metal injection and AGN feedback (Sijacki et al. 2007; Roediger et al. 2007) but also cosmic-ray injection, anisotropic transport and cosmic-ray diffusion. By modifying the convective instability criterion these three last ingredients should drive turbulence to a level close to the one predicted by the mixing length theory.

This work was partially supported by NASA's Astrophysical Theory Program under grant NNG 05GH39G and by NSF under grant AST 05-49577. We acknowledge the usage of the HyperLeda database (<http://leda.univ-lyon1.fr>).

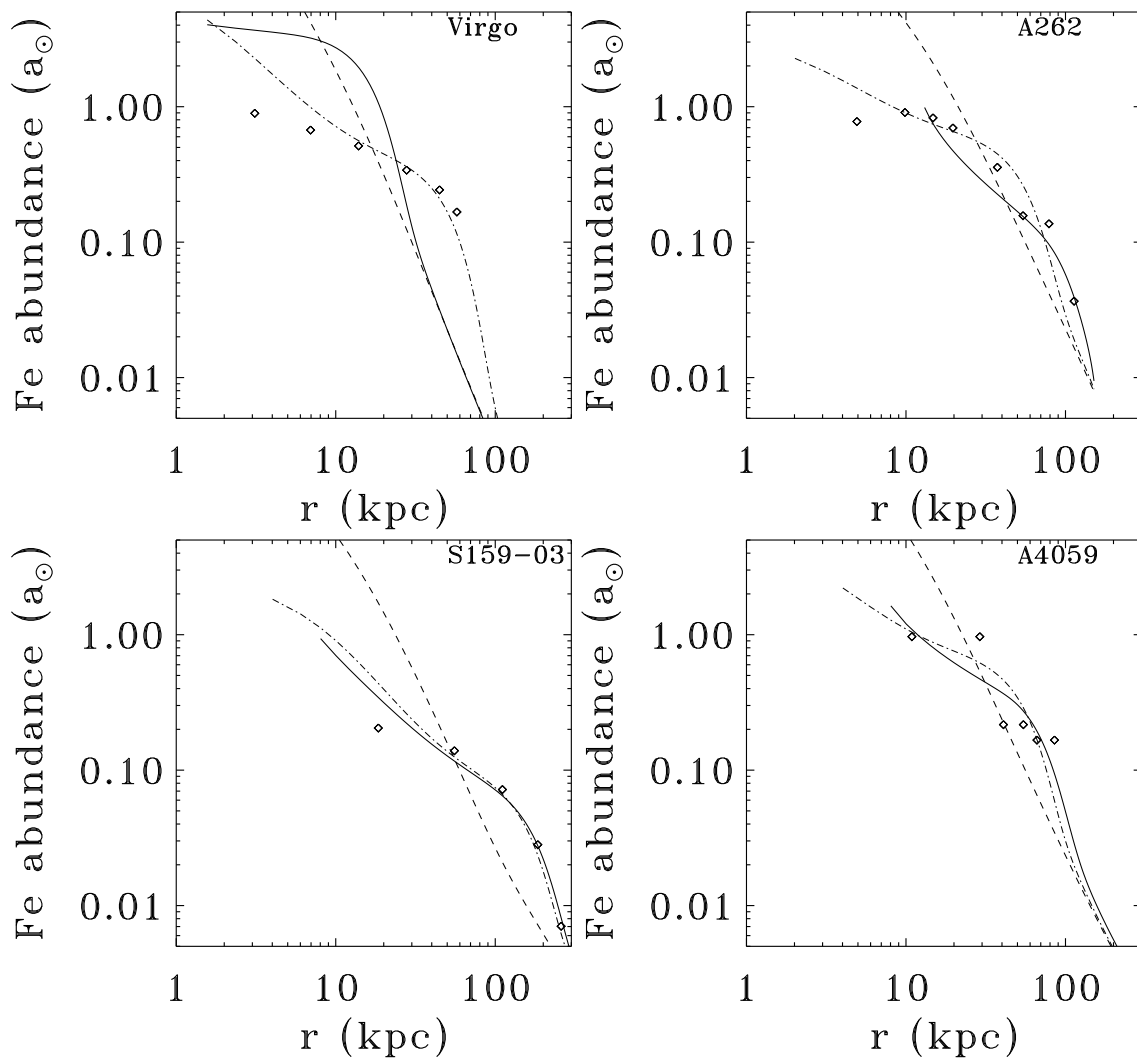


Fig. 3.— Abundance profile in solar unit as a function of the radius in kpc for Virgo, Abell 262, Sersic 159-03, and Abell 4059. The dashed line is the resulting abundance profile without diffusion. The continuous line is the resulting profile with the present cluster diffusion. The dot-dashed line is the profile with the best fit cosmic-ray luminosity value and subsequent diffusion. The diamonds are the observations. Past and present AGN-driven convection seems to play an important role for the transport of iron.

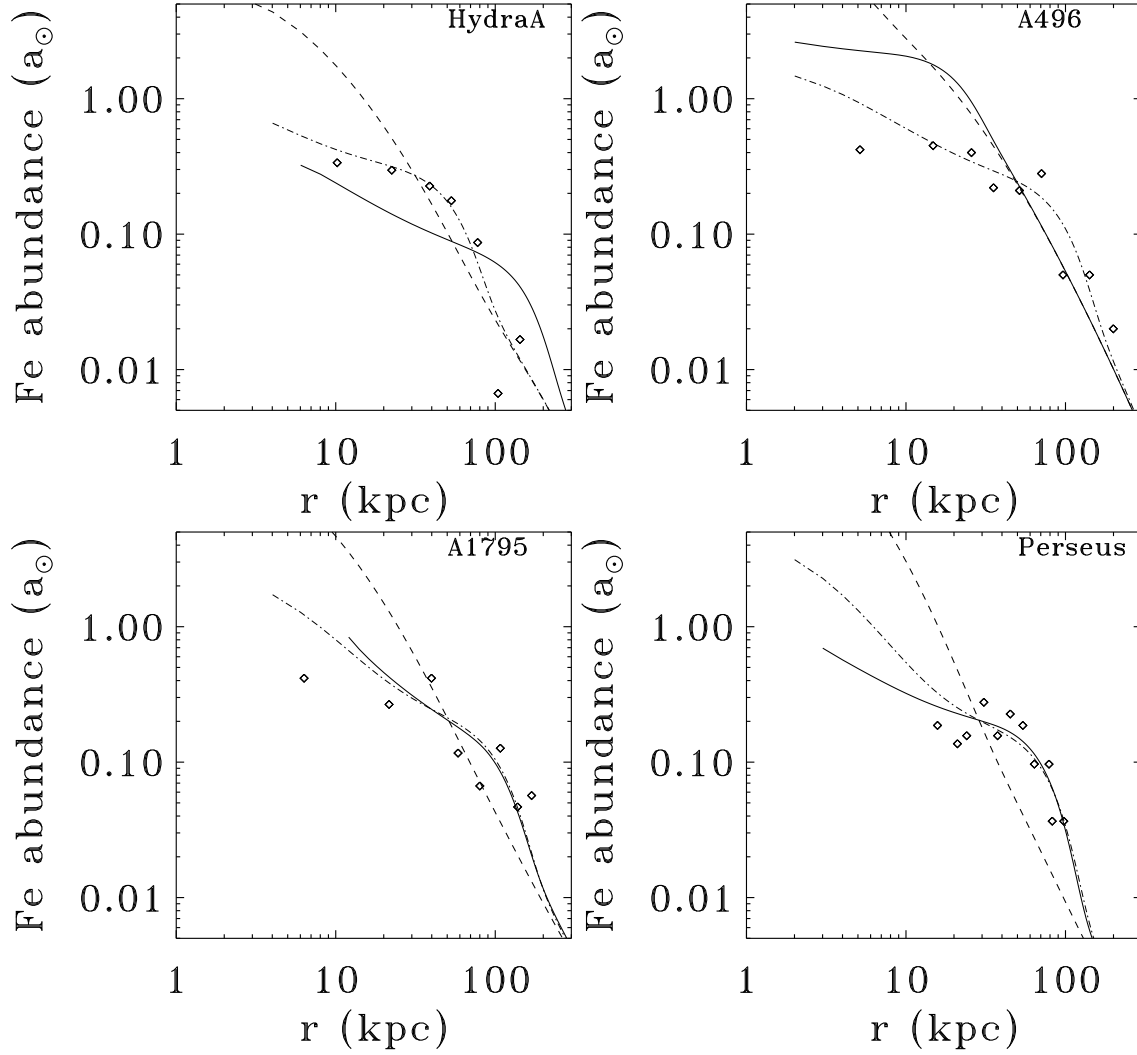


Fig. 4.— Abundance profile in solar unit as a function of the radius in kpc for Hydra A, Abell 496, Abell 1795, and Perseus. The dashed line is the resulting abundance profile without diffusion. The continuous line is the resulting profile with the present cluster diffusion. The dot-dashed line is the profile with the best fit cosmic-ray luminosity value and subsequent diffusion. The diamonds are the observations. Past and present AGN-driven convection seems to play an important role for the transport of iron.

REFERENCES

- Allen, S. W., Dunn, R. J. H., Fabian, A. C., Taylor, G. B., & Reynolds, C. S. 2006, *MNRAS*, 372, 21
- Anders, E., & Grevesse, N. 1989, *Geochim. Cosmochim. Acta*, 53, 197
- Balbus, S. A. 2000, *ApJ*, 534, 420
- Balbus, S. A. 2001, *ApJ*, 562, 909
- Ball, R., Burns, J. O., & Loken, C. 1993, *AJ*, 105, 53
- Begelman, M. C. 2001, *Gas and Galaxy Evolution*, 240, 363
- Best, P. N., von der Linden, A., Kauffmann, G., Heckman, T. M., & Kaiser, C. R. 2007, *MNRAS*, 527
- Binney, J., & Tabor, G. 1995, *MNRAS*, 276, 663
- Birzan, L., Rafferty, D. A., McNamara, B. R., Wise, M. W., & Nulsen, P. E. J. 2004, *ApJ*, 607, 800
- Blanton, E. L., Sarazin, C. L., & McNamara, B. R. 2003, *ApJ*, 585, 227
- Blandford, R., & Begelman, M. 1999, *MNRAS*, 303, L1
- Boehringer, H., & Morfill, G. E. 1988, *ApJ*, 330, 609
- Böhringer, H., et al. 2001, *A&A*, 365, L181
- Böhringer, H., Matsushita, K., Churazov, E., Finoguenov, A., & Ikebe, Y. 2004, *A&A*, 416, L21
- Borriello, A., Salucci, P., & Danese, L. 2003, *MNRAS*, 341, 1109
- Brüggen, M., Kaiser, C. R., Churazov, E., & Enßlin, T. A. 2002, *MNRAS*, 331, 545
- Brüggen, M., & Kaiser, C. R. 2002, *Nature*, 418, 301
- Brüggen, M. 2003, *ApJ*, 592, 839
- Brüggen, M., Ruszkowski, M., & Hallman, E. 2005, *ApJ*, 630, 740
- Burns, J. O. 1990, *AJ*, 99, 14
- Cappellaro, E., Evans, R., & Turatto, M. 1999, *A&A*, 351, 459
- Carollo, C. M., Franx, M., Illingworth, G. D., & Forbes, D. A. 1997, *ApJ*, 481, 710
- Cattaneo, A., & Teyssier, R. 2007, *MNRAS*, 376, 1547
- Chandran, B. D. G., & Cowley, S. C. 1998, *Physical Review Letters*, 80, 3077
- Chandran, B. D. G., & Maron, J. L. 2004, *ApJ*, 602, 170
- Chandran, B. D. G. 2005, *ApJ*, 632, 809
- Chandran, B. D., & Dennis, T. J. 2006, *ApJ*, 642, 140
- Chandran, B. D. G., & Rasera, Y. 2007, *ApJ*, 671, 1413
- Cho, J., Lazarian, A., Honein, A., Knaepen, B., Kassinos, S., & Moin, P. 2003, *ApJ*, 589, L77
- Choi, Y.-Y., Reynolds, C. S., Heinz, S., Rosenberg, J. L., Perlman, E. S., & Yang, J. 2004, *ApJ*, 606, 185
- Churazov, E., Brüggen, M., Kaiser, C. R., Böhringer, H., & Forman, W. 2001, *ApJ*, 554, 261
- Churazov, E., Böhringer, H., Brüggen, M., Forman, W., Jones, C., Kaiser, C., & Sunyaev, R. 2002, *Lighthouses of the Universe: The Most Luminous Celestial Objects and Their Use for Cosmology*, 37
- Churazov, E., Forman, W., Jones, C., Böhringer, H. 2003, *ApJ*, 590, 225
- Churazov, E., Forman, W., Jones, C., Sunyaev, R., Böhringer, H. 2004, *MNRAS*, 347, 29
- Ciotti, L., Pellegrini, S., Renzini, A., & D’Ercole, A. 1991, *ApJ*, 376, 380
- Ciotti, L., & Ostriker, J. P. 1997, *ApJ*, 487, L105
- Ciotti, L., & Ostriker, J. P. 2001, *ApJ*, 551, 131
- Ciotti, L., Ostriker, J. P., & Pellegrini, S. 2004, *Plasmas in the Laboratory and in the Universe: New Insights and New Challenges*, 703, 367

- David, L. P., Nulsen, P. E. J., McNamara, B. R., Forman, W., Jones, C., Ponman, T., Robertson, B., & Wise, M. 2001, *ApJ*, 557, 546
- Dennis, T. J., & Chandran, B. D. G. 2004, *Bulletin of the American Astronomical Society*, 36, 1592
- Dennis, T. J., & Chandran, B. D. G. 2004 2005, *ApJ*, 622, 205
- Dennis, T. J., & Chandran, B. D. 2007, *ApJ*, submitted
- de Plaa, J., et al. 2006, *A&A*, 452, 397
- De Grandi, S., & Molendi, S. 2001, *ApJ*, 551, 153
- de Vaucouleurs, G. 1953, *MNRAS*, 113, 134
- Di Matteo, T., Colberg, J., Springel, V., Hernquist, L., & Sijacki, D. 2007, *ArXiv e-prints*, 705, arXiv:0705.2269
- Donahue, M., Horner, D. J., Cavagnolo, K. W., & Voit, G. M. 2006, *ApJ*, 643, 730
- Ettori, S., Fabian, A. C., Allen, S. W., & Johnstone, R. M. 2002, *MNRAS*, 331, 635
- Eilek, J. A. 2004, *The Riddle of Cooling Flows in Galaxies and Clusters of galaxies*, 165
- El-Zant, A. A., Kim, W.-T., & Kamionkowski, M. 2004, *MNRAS*, 354, 169
- Fabian, A. C. 1994, *ARA&A*, 32, 277
- Fabian, A. C., Voigt, L. M., & Morris, R. G. 2002, *MNRAS*, 335, L71
- Fabian, A. C., Sanders, J. S., Allen, S. W., Crawford, C. S., Iwasawa, K., Johnstone, R. M., Schmidt, R. W., & Taylor, G. B. 2003, *MNRAS*, 344, L43
- Fabian, A. C., Sanders, J. S., Crawford, C. S., Conselice, C. J., Gallagher, J. S., & Wyse, R. F. G. 2003, *MNRAS*, 344, L48
- Finoguenov, A., Matsushita, K., Böhringer, H., Ikebe, Y., & Arnaud, M. 2002, *A&A*, 381, 21
- Forman, W., et al. 2005, *ApJ*, 635, 894
- Graham, A., Lauer, T. R., Colless, M., & Postman, M. 1996, *ApJ*, 465, 534
- Graham, J., Fabian, A. C., Sanders, J. S., & Morris, R. G. 2006, *MNRAS*, 368, 1369
- Häring, N., & Rix, H.-W. 2004, *ApJ*, 604, L89
- Heinz, S., Brüggen, M., Young, A., & Levesque, E. 2006, *MNRAS*, 373, L65
- Hernquist, L. 1990, *ApJ*, 356, 359
- Hoeft, M., & Brüggen, M. 2004, *ApJ*, 617, 896
- Jimenez, R., Bernardi, M., Haiman, Z., Panter, B., & Heavens, A. F. 2007, *ApJ*, 669, 947
- Kaastra, J. S., et al. 2004, *A&A*, 413, 415
- Kim, W.-T., El-Zant, A. A., & Kamionkowski, M. 2005, *ApJ*, 632, 157
- Kim, W.-T., & Narayan, R. 2003, *ApJ*, 596, L139
- Loewenstein, M., & Fabian, A. C. 1990, *MNRAS*, 242, 120
- Loewenstein, M., Zweibel, E. G., & Begelman, M. C. 1991, *ApJ*, 377, 392
- McNamara, B. R. 2004, *The Riddle of Cooling Flows in Galaxies and Clusters of galaxies*, 177
- Makishima, K., et al. 2001, *PASJ*, 53, 401
- Matsushita, K., Belsole, E., Finoguenov, A., Böhringer, H. 2002, *A&A*, 386, 77
- Molendi, S., & Pizzolato, F. 2001, *ApJ*, 560, 194
- Narayan, R., & Medvedev, M. V. 2001, *ApJ*, 562, L129
- Narayan, R., & Kim, W.-T. 2004, *Frontier in Astroparticle Physics and Cosmology*, 183
- Omma, H., & Binney, J. 2004, *MNRAS*, 350, L13
- Omma, H., Binney, J., Bryan, G., & Slyz, A. 2004, *MNRAS*, 348, 1105
- Parker, E. N. 1966, *ApJ*, 145, 811
- Parrish, I. J., & Stone, J. M. 2005, *ApJ*, 633, 334
- Parrish, I. J., & Stone, J. M. 2007, *ApJ*, 664, 135
- Parrish, I., & Quataert, E. 2008, *ApJL*, 677, L9

- Paturel, G., Petit, C., Prugniel, P., Theureau, G., Rousseau, J., Brouty, M., Dubois, P., & Cambr sy, L. 2003, *A&A*, 412, 45
- Peterson, J. R., et al. 2001, *A&A*, 365, L104
- Peterson, J. R., Kahn, S. M., Paerels, F. B. S., Kaastra, J. S., Tamura, T., Bleeker, J. A. M., Ferrigno, C., & Jernigan, J. G. 2003, *ApJ*, 590, 207
- Pope, E. C. D., Pavlovski, G., Kaiser, C. R., & Fangohr, H. 2006, *MNRAS*, 367, 1121
- Pope, E. C. D. 2007, *ArXiv e-prints*, 707, arXiv:0707.2597
- Quataert, E., & Narayan, R. 2000, *ApJ*, 528, 236
- Quataert, E. 2008, *ApJ*, 673, 758
- Quilis, V., Bower, R. G., & Balogh, M. L. 2001, *MNRAS*, 328, 1091
- Rafferty, D. A., McNamara, B. R., Nulsen, P. E. J., & Wise, M. W. 2006, *ApJ*, 652, 216
- Rasera, Y. & Chandran, B. D. 2008, *ApJ*, in press
- Rebusco, P., Churazov, E., B hringer, H., & Forman, W. 2005, *MNRAS*, 359, 1041
- Rebusco, P., Churazov, E., B hringer, H., & Forman, W. 2006, *MNRAS*, 372, 1840
- Renzini, A., Ciotti, L., D’Ercole, A., & Pellegrini, S. 1993, *ApJ*, 419, 52
- Reynolds, C. S., Heinz, S., & Begelman, M. C. 2001, *ApJ*, 549, L179
- Reynolds, C. S., Heinz, S., & Begelman, M. C. 2002, *MNRAS*, 332, 271
- Reynolds, C. S., McKernan, B., Fabian, A. C., Stone, J. M., & Vernaleo, J. C. 2005, *MNRAS*, 357, 242
- Roediger, E., Br ggen, M., Rebusco, P., B hringer, H., & Churazov, E. 2007, *MNRAS*, 375, 15
- Rosner, R., & Tucker, W. H. 1989, *ApJ*, 338, 761
- Ruszkowski, M., & Begelman, M. C. 2002, *ApJ*, 581, 223
- Ruszkowski, M., Br ggen, M., & Begelman, M. C. 2004, *ApJ*, 611, 158
- Ruszkowski, M., Br ggen, M., & Begelman, M. C. 2004, *ApJ*, 615, 675
- Sadat, R., Blanchard, A., Kneib, J.-P., Mathez, G., Madore, B., & Mazzarella, J. M. 2004, *A&A*, 424, 1097
- Sazonov, S. Y., Ostriker, J. P., Ciotti, L., & Sunyaev, R. A. 2005, *MNRAS*, 358, 168
- Schombert, J. M. 1987, *ApJS*, 64, 643
- Schombert, J. M. 1988, *ApJ*, 328, 475
- Sijacki, D., & Springel, V. 2006, *MNRAS*, 371, 1025
- Sijacki, D., Springel, V., Di Matteo, T., & Hernquist, L. 2007, *ArXiv e-prints*, 705, arXiv:0705.2238
- Tabor, G., & Binney, J. 1993, *MNRAS*, 263, 323
- Tamura, T., Bleeker, J. A. M., Kaastra, J. S., Ferrigno, C., & Molendi, S. 2001, *A&A*, 379, 107
- Tamura, T., et al. 2001, *A&A*, 365, L87
- Tan, J. C., & Blackman, E. G. 2005, *MNRAS*, 362, 983
- Tribble, P. C. 1989, *MNRAS*, 238, 1247
- Vernaleo, J. C., & Reynolds, C. S. 2006, *ApJ*, 645, 83
- Vikhlinin, A., Markevitch, M., Murray, S. S., Jones, C., Forman, W., & Van Speybroeck, L. 2005, *ApJ*, 628, 655
- Voigt, L. M., Schmidt, R. W., Fabian, A. C., Allen, S. W., & Johnstone, R. M. 2002, *MNRAS*, 335, L7
- Voigt, L. M., & Fabian, A. C. 2004, *MNRAS*, 347, 1130
- Voit, G. M., & Donahue, M. 2005, *ApJ*, 634, 955
- Werner, N., Kaastra, J. S., Takei, Y., Lieu, R., Vink, J., & Tamura, T. 2007, *A&A*, 468, 849
- Zakamska, N. L., & Narayan, R. 2003, *ApJ*, 582, 162

This 2-column preprint was prepared with the AAS L^AT_EX macros v5.2.

Cluster	z	M_{vir} ($h^{-1}M_{\odot}$)	L_{cr} ($erg.s^{-1}$)	BCG	L_B (L_{\odot}^B)	r_e (kpc)
Virgo	0.00372	3.1×10^{14}	5.8×10^{41}	M87	6.4×10^{10}	6.1
Abell262	0.0155	3.2×10^{13}	6.6×10^{42}	NGC708	3.8×10^{10}	24
Sersic159-03	0.0572	9.6×10^{13}	1.1×10^{44}	ESO291-009	1.3×10^{11}	27
Abell4059	0.0466	6.8×10^{14}	1.7×10^{43}	ESO349-010	1.9×10^{11}	22
HydraA	0.0550	7.1×10^{13}	2.4×10^{44}	3C218	2.6×10^{11}	44
Abell496	0.0322	8.2×10^{13}	1.9×10^{42}	PGC015524	1.6×10^{11}	50
Abell1795	0.0639	5.0×10^{14}	1.0×10^{44}	PGC049005	1.1×10^{11}	42
Perseus	0.0179	6.2×10^{14}	9.8×10^{43}	NGC1275	1.7×10^{11}	15

Table 1: Clusters and BCGs general properties

NOTE.—z is the redshift, M_{vir} is the virial mass, L_{cr} is the cosmic-ray luminosity (AGN power), BCG is the brightest cluster galaxy, L_B is the blue luminosity of the BCG and r_e is the effective radius which contains half the projected luminosity. Methods, definitions and references are described in section 4.

Cluster	r_{max} (kpc)	D_{max} ($cm^2.s^{-1}$)	r_b (kpc)	a_b (a_{\odot})	M_{Fe} (M_{\odot})	$r_{1/2}$ (kpc)
Virgo	4.4	8.0×10^{27}	58	0.20	4.2×10^7	36
Abell262	62	6.3×10^{28}	200	0.29	1.4×10^8	55
Sersic159-03	98	2.6×10^{29}	260	0.14	2.4×10^8	110
Abell4059	39	4.7×10^{28}	85	0.43	1.9×10^8	44
HydraA	78	2.5×10^{29}	140	0.28	2.0×10^8	57
Abell496	7.8	8.0×10^{27}	200	0.28	2.6×10^8	80
Abell1795	67	9.9×10^{28}	170	0.33	4.8×10^8	92
Perseus	30	9.4×10^{28}	98	0.46	1.7×10^8	53

Table 2: Diffusion properties derived in the AGN-convection model and abundance profile parameters

NOTE.— r_{max} is the position of the maximum of the diffusion coefficient and D_{max} is the maximum. r_b is the radius of the last bin of the observed abundance profile, a_b is the background abundance (relative to the solar abundance of Anders & Grevesse (1989)) which is subtracted to the abundance profile to obtain the iron excess, M_{Fe} is the total observed iron mass, and $r_{1/2}$ is the iron half mass radius (which therefore contains an iron mass of $M_{Fe}/2$). Methods, definitions and references are described in section 4.

Cluster	L_{cr}^{fit} (erg.s ⁻¹)	r_{max}^{fit} (kpc)	D_{max}^{fit} (cm ² .s ⁻¹)	sr_{eff} SNU	$r_{1/2}^{fit}$ (kpc)
Virgo	1.0×10^{43}	23	3.8×10^{28}	0.082	33
Abell262	1.0×10^{43}	24	3.8×10^{28}	0.21	47
Sersic159-03	2.0×10^{44}	87	2.1×10^{29}	0.19	99
Abell4059	1.0×10^{43}	23	3.8×10^{28}	0.11	44
HydraA	1.0×10^{43}	23	3.8×10^{28}	0.082	54
Abell496	5.0×10^{43}	48	9.6×10^{28}	0.17	79
Abell1795	7.0×10^{43}	55	1.2×10^{29}	0.43	81
Perseus	3.0×10^{43}	37	7.1×10^{28}	0.11	51

Table 3: AGN power and diffusion properties for the best fit model to the abundance profile

NOTE.— L_{cr}^{fit} is the cosmic-ray luminosity (AGN power) required to reproduce the observed abundance profile. From this AGN power, we derived the diffusion coefficient profile. r_{fit}^{max} is the radius of the maximum of the diffusion coefficient profile and D_{fit}^{max} is the maximum. sr_{eff} is the effective SNIa rate (which includes the wind contribution to the iron injection). $r_{1/2}^{fit}$ is the iron half mass radius of the model (which contains half the total iron mass inside r_b). Methods and definitions are described in section 2 and section 6.